Surface modes with controlled axisymmetry triggered by bubble coalescence in a high-amplitude acoustic field

Sarah Cleve,[1,*] Matthieu Guédra,[2] Claude Inserra,[2] Cyril Mauger,[1] and Philippe Blanc-Benon[1]
[1]*Univ Lyon, École Centrale de Lyon, INSA de Lyon, CNRS, LMFA UMR 5509, F-69134 Écully, France*
[2]*Univ Lyon, Université Claude Bernard Lyon 1, Centre Léon Bérard, INSERM, UMR 1032, LabTAU, F-69003, Lyon, France*

(Received 6 October 2017; published 24 September 2018)

When two bubbles encounter each other in a moderate ultrasound field they coalesce into a single bubble that shows purely spherical oscillations. For a sufficiently large acoustic field, this coalescence can lead to sustained nonspherical oscillations of the resulting bubble. We experimentally capture the time-resolved dynamics of the coalesced bubble, starting with the moment of film rupture. This allows the transient and steady-state regimes of the oscillating bubble to be studied. The amplitude dynamics for both of these regimes are successfully compared to numerical modeling, taking into account the coupling of volume and surface modes. Initial conditions for each surface mode are taken from the Legendre polynomial projection of the experimentally obtained bubble shape immediately after film rupture. We also observe that the symmetry axis of the zonal spherical harmonics is defined by the coalescence. The axis is identical to the rectilinear translational motion of the two approaching bubbles before impact. This high-amplitude coalescence technique provides a unique opportunity to study axisymmetric and sustained nonspherical bubble oscillations under controlled initial conditions.

DOI: 10.1103/PhysRevE.98.033115

I. INTRODUCTION

Extensive efforts have been devoted to the theoretical investigation of nonspherical bubble oscillations, which historically have been due to their importance in describing the mechanisms underlying bubble sonoluminescence [1–4]. In the first studies, the shape stability and distorsion amplitude were described according to uncoupled mode theories [1], which correctly characterized the onset of surface mode emergence but neglected possible nonlinear saturation effects of surface mode amplitude. The models were later extended to account for energy transfer between translational, spherical, and surface modes [5–8], which therefore included inhibition of shape perturbation growth. In the context of biomedical applications, shape-oscillating bubbles are promising vectors for microstreaming enhancement and drug delivery processes [9,10]. The latest analytical developments on surface instabilities hence included the shell behavior of ultrasound contrast agents [11–13] and the description of shape-induced microstreaming patterns for transport and mixing processes [5,14]. In contrast to theoretical approaches, only a few experimental studies have focused on the analysis of bubble surface oscillations, as they had to cope with the intrinsic difficulties linked to bubble instabilities. Among these, translational instabilities and diverging amplitudes of nonspherical modes have been used to investigate bubbles submitted to short acoustic pulses [15,16]. These studies were centered almost exclusively on the pressure threshold p_{th}^{n} above which a bubble will show a given surface mode n, with the temporal dynamics of nonspherical oscillations only described qualitatively. A recent alternative approach consisted of driving bubbles with an amplitude-modulated ultrasound field, while allowing periodic onset and extinction of shape modes [17]. Nonspherical oscillations were therefore excited over a sufficiently long duration (in terms of the acoustic timescale) to enable the capture of the temporal dynamics and the observation of nonlinear mode coupling [18]. Experimental difficulties are the positional stability of the bubble as well as the appropriate observation of bubble shape modes (possibly decomposed on spherical harmonics with out-of-plane deformations). To overcome such difficulties, attention is usually paid to the controlled trapping of the bubbles using optical tweezers [15,19]. The bubbles are then subjected to propagating ultrasound waves that define the symmetry axis of nonspherical oscillations [20]. In all cases, experimental studies on temporal dynamics or threshold determination are based on the emergence of surface mode instability from an initially spherical bubble. An interesting alternative would consist of driving initially deformed bubbles with a sufficiently strong ultrasound field to sustain surface modes. Such initial states of deformations can be obtained through the process of bubble coalescence.

Summed up very briefly, the process of bubble coalescence can be divided into (1) bubble encounter, (2) formation of a thin liquid film between the two bubbles, (3) film rupture, and (4) establishment of a steady-state regime. Most of the existing literature reports on the hydrodynamic coalescence of rising bubbles and focuses on the bubble approach [21], film drainage [22], and bouncing behavior [23]. Analysis of micrometric colliding bubbles revealed the surface dynamics of the resulting bubble, whereby the coalescence is followed by large-amplitude ellipsoidal deformation, before relaxation into the spherical shape [24]. Recently, bubble coalescence was investigated by applying an ultrasound field so that the main force ruling the approach and collision of the bubbles became the primary (radiation) and secondary (mutual

*sarah.cleve@ec-lyon.fr

interaction) Bjerknes forces acting on the bubbles [25]. The main findings were an increase in the coalescence time for free micrometric bubbles [26], which led to modification of the film drainage theory [27]. These studies were all carried out in a relatively low ultrasound field, and consequently, the coalesced bubble returned to purely spherical oscillations.

In the present paper, we take advantage of the process of bubble coalescence in a sufficiently strong acoustic field, to initiate and sustain large-amplitude surface deformation. Control of the symmetry axis for nonspherical oscillations is demonstrated. The temporal dynamics of surface oscillations from the film rupture to their steady-state regime are captured, and the shape mode amplitudes are successfully recovered through recent theories that account for mode coupling.

II. EXPERIMENTAL SETUP AND PROCEDURES

A schematic of the experimental setup is given in Fig. 1(a). The experiments are conducted on gas bubbles in bidistilled nondegassed water. The experimental setup consists of an 8-cm-edge cubic water tank. Single bubbles are nucleated by focused laser pulses [$\lambda = 532$ nm, second harmonic of a Nd:YAG pulsed laser (New Wave Solo III); pulse duration, 6 ns]. The size of the nucleated bubbles can be influenced slightly by tuning the energy of the laser pulse. The bubbles are trapped in the acoustic field induced by an ultrasonic plane transducer (SinapTec; diameter of active area, 35 mm). The voltage amplitude of the transducer is varied between 1 V and 6 V, with no gain amplifier used. All of the experiments are conducted at a driving frequency set to 31.25 kHz, which corresponds to a resonant radius $R_{\text{res}} \approx 104\,\mu$m, following Minnaert's theory [28].

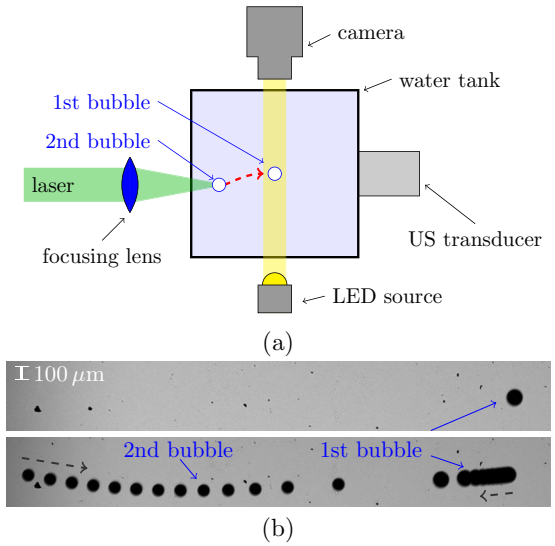

FIG. 1. (a) Schematic presentation of the experimental setup. (b) Visualization of the bubble trajectories before coalescence: a single bubble is trapped at a stable position in the acoustic field (top half); once a second bubble is approaching from the left, the two of them will be attracted towards each other due to secondary Bjerknes forces (bottom half, superposition of several photos). The moment of coalescence is not shown here but will be discussed in the following sections. Once the bubbles have coalesced, the new bubble will return to a stable position.

Experiments are captured with a CMOS camera (Vision Research, v.12.1) equipped with a 12× objective lens (Navitar). Backlight illumination is assured by a continuous light-emitting diode (LED) light source. A frame size of 256 × 256 pixels is used to allow a frame rate of 67.065 kHz. For this setup, the depth of field of the camera objective and lenses is about 200 μm.

Each experiment is conducted as follows [Fig. 1(a)]: One bubble is nucleated at a few millimeters from a pressure antinode of the acoustic field. The bubble is then driven toward, and trapped at, the antinode, due to primary Bjerknes forces of the acoustic field on the bubble. A second bubble is nucleated, and its trajectory [see example in Fig. 1(b)] is influenced by primary Bjerknes forces and by secondary Bjerknes forces between the two bubbles. The coalescence is captured, covering the approach of the two bubbles, their impact, and the coalesced bubble. Eighty experiments were conducted, with radii of the coalesced bubbles ranging from 30 μm to 90 μm. If desired, a trapped bubble can be grown by multiple coalescence. All of the bubbles are below resonant size. Uncertainties on the radius are mainly due to the pixel size and the image-processing parameters, and they are estimated as $\pm 3\,\mu$m. For experiments where two spherical bubbles coalesce into a single spherical one, conservation of volume, as $V_1 + V_2 = V_{\text{coal}}$, has been verified.

Acoustic field characterization: The acoustic pressure is deduced from the bubble dynamics in a relatively weak acoustic field as follows. When one single bubble is trapped at the pressure antinode at sufficiently low acoustic pressure, it shows only spherical oscillations. Typical bubble wall expansions can reach 10% of the equilibrium radius depending on the applied voltage. By capturing the radial dynamics over a sufficiently long time and then rearranging it on a single acoustic period, the obtained waveform can be numerically compared to the Keller-Miksis modeling [29]. As all other parameters are known or can be measured directly, the acoustic pressure can then be deduced from the modeling. Using the model for a large number of single bubbles, a linear relationship was obtained between the transducer voltage applied and the acoustic pressure. The acoustic pressure ranges between 5 kPa and 35 kPa, with a ±5 kPa uncertainty.

Surface mode analysis: The centroid and the bubble contour are extracted by image processing. For each frame that corresponds to the time t, the contour can be described by $r_s(\theta, t)$ using the polar coordinates (r_s, θ), with the origin at the centroid [see Fig. 2(a)].

Care has to be taken to correctly define the symmetry axis of the bubble. Our findings on the definition of the symmetry axis will be discussed in Sec. III. Assuming axial symmetry, the decomposition in Legendre polynomials P_n according to

$$r_s(\theta, t) = \sum_{n=0}^{4} a_n(t) P_n(\cos\theta) \tag{1}$$

allows computation of the modal coefficients $a_n(t)$ [18]:

$$a_n(t) = \frac{2n+1}{2} \int_{-1}^{1} r_s(x, t) P_n(x)\, dx \quad \text{with} \quad x = \cos\theta\,. \tag{2}$$

The coefficient $a_0(t)$ corresponds to the volume pulsations of the bubble, noted as $R(t)$ in the following. The coefficient

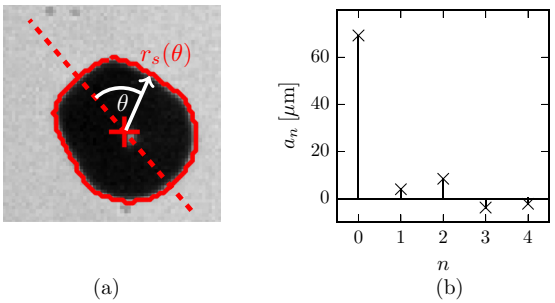

FIG. 2. (a) Definition of the bubble shape $r_s(\theta)$. (b) The associated modal decomposition. This example corresponds to a bubble of $R_0 = 68.1\,\mu$m [one snapshot from the series in Fig. 3(c), frame size $220\,\mu\text{m} \times 220\,\mu$m]. The modal decomposition gives one single measurement point of the complete graph that will be shown in Fig. 7.

$a_1(t)$ can be related to translational oscillations, which were negligible in the present study. The amplitudes of the shape modes 2, 3, and 4 are expressed by $a_2(t)$, $a_3(t)$, and $a_4(t)$. Figure 2(b) shows an example of modal decomposition of the bubble shape shown in Fig. 2(a), which highlights the predominance of the second mode.

III. TRIGGERING OF SURFACE MODES BY BUBBLE COALESCENCE

Most of the existing papers report on studies of ultrasound-induced bubble coalescence in a relatively weak ultrasound field, thus corresponding to acoustic pressures too low to initiate the parametric excitation of shape modes. This case of a bubble returning to spherical shape is illustrated in Fig. 3(a).

When two bubbles approach, a thin liquid film forms between the bubbles as soon as they are sufficiently close. The rupture of this film can be interpreted as the first moment at which one single bubble exists, with an initial shape deformation (Fig. 3, red box). We therefore assigned the time $t = 0\,\mu$s to the first image on which the liquid film has ruptured. This initial deformation is followed by a transient regime (Fig. 3, blue box, two consecutive snapshots), before reaching a steady-state regime (Fig. 3, green box, four consecutive snapshots). For the low-pressure example in Fig. 3(a), the steady-state regime shows a purely spherical mode oscillation. When carried out in a stronger acoustic field, bubble coalescence can lead to nonspherical oscillations of the resulting bubble. Such oscillations classically appear if the acoustic pressure exceeds a critical threshold $p^n_{\text{th}}(R_{0,\text{coal}})$, above which a specific surface mode becomes unstable. Note that because our experiments are conducted at a fixed driving frequency, this threshold mainly depends on the static radius of the bubble $R_{0,\text{coal}}$ and on the considered shape mode number n. Examples of nonspherical oscillations triggered by bubble coalescence are presented in Figs. 3(b)–3(d), where different shape modes are obtained in the steady-state regime: (b) $n = 2$, (c) $n = 3$, and (d) $n = 4$. The corresponding bubble sizes and acoustic pressures are summarized in Table I. For example, Fig. 3(c) shows oscillations of the third shape mode obtained from two bubbles of respective radii $R_{0,1} \simeq 63\,\mu$m and $R_{0,2} \simeq 26\,\mu$m coalescing into one single bubble of radius $R_{0,\text{coal}} \simeq 68\,\mu$m. The amplitude of the acoustic field is $P_a = 10.4\,$kPa for this case, which is indeed larger than the predicted pressure threshold $p^3_{\text{th}} \simeq 6.6\,$kPa (theory based on Ref. [1]) for parametric excitation of the third shape mode for this given bubble radius. The entire set of these coalescence

TABLE I. Bubble size, acoustic pressure, and pressure thresholds of mode n for the cases of bubble coalescence presented in Fig. 3.

	$R_{0,1}$ [μm]	$R_{0,2}$ [μm]	$R_{0,\text{coal}}$ [μm]	p_{ac} [kPa]	n	p^n_{th} [kPa]
(a)	25.3	30.3	39.5	14.8	-	-
(b)	40.3	19.8	44.9	30.6	2	16.4
(c)	62.9	26.2	68.1	10.4	3	6.6
(d)	49.2	32.6	53.6	24.1	4	6.5

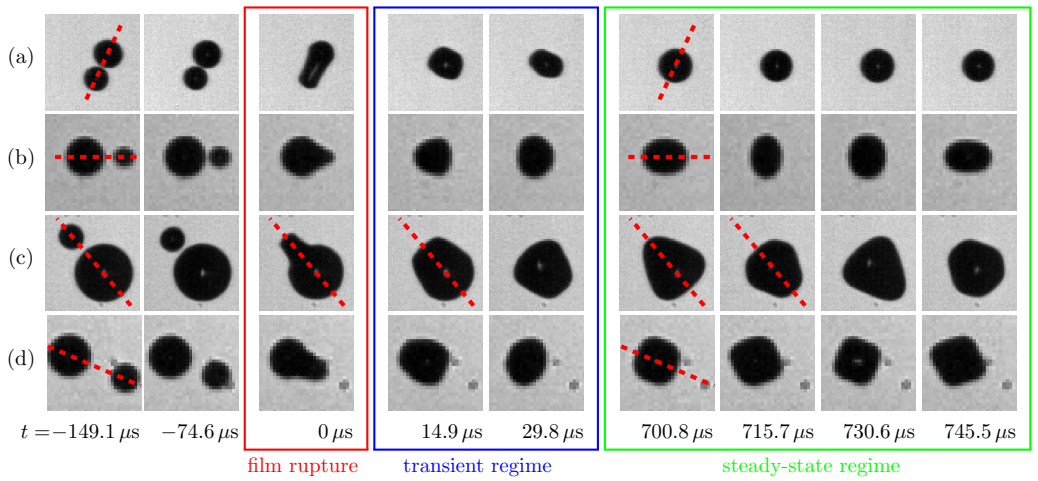

FIG. 3. Extracts of two coalescing bubbles that result in a single bubble with different modes: (a) spherical mode, (b) mode 2, (c) mode 3, and (d) mode 4. The reference time of $0\,\mu$s corresponds to the first image after the film rupture, indicated by the red box. The frames presented here have a height and width of $220\,\mu$m. The bubble sizes are summarized in Table I. The corresponding videos can be found in the Supplemental Material [30].

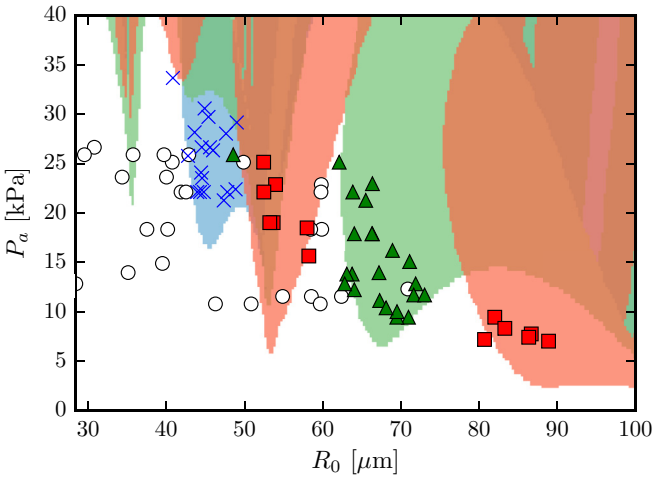

FIG. 4. Pressure-radius diagram showing the different modes of the coalesced bubbles in the established regime. ○, spherical mode; ×, mode 2; △, mode 3; □, mode 4. The background colors correspond to the analytical solutions: white, spherical mode; blue, mode 2; green, mode 3; red, mode 4.

recordings is summarized in a stability diagram shown in Fig. 4. Good agreement is obtained between the experiments (symbols) and the predicted stable zones of the shape modes (background colors; theory based on Ref. [1]). Experimental points are focused around the stability thresholds. Pressures that are too low are without interest for the purpose of the study (spherical oscillations only). In contrast, pressures that are too large (compared to the stability threshold of a given shape mode) lead to difficulties in observing the bubbles due to the onset of positional instabilities.

Bubble coalescence is a rapid and reliable technique to trigger surface oscillations of large amplitude. Indeed, shape-oscillating microbubbles are usually investigated by gradually increasing the acoustic amplitude until the parametric excitation threshold is reached [18,31]. This generally leads to translational instabilities in the bubble motion when sufficiently large driving amplitudes are reached [32]. Another approach to investigate surface oscillations is by short ultrasound bursts [20]; however, this does not allow for steady-state observations. Through bubble coalescence, large-amplitude nonspherical oscillations can be reached in a single step, thus allowing straightforward investigations of their nonlinear properties. This will be discussed in Sec. IV.

In addition, all existing theories that account for nonspherical oscillations of bubbles assume shape axisymmetry, a hypothesis that is usually considered as fulfilled experimentally by considering that shape symmetry is defined by the direction of the traveling ultrasound beam. The axisymmetry property and its impact on the correct modal decomposition of the bubble apparent contour was recently investigated in Ref. [33]. Importantly, the present study reveals that bubble coalescence in a standing ultrasound beam leads to unambiguous definition of the axis of symmetry of the nonspherical bubble by the impact axis between the two initial bubbles. This is illustrated in Fig. 3, where the impact axis of the two approaching bubbles and the symmetry axis of the coalesced bubble are represented by straight dashed lines. Far from being obvious at first glance, this phenomenon allows control of the surface mode orientation. By controlling the initial locations and velocities of the bubbles in a way that their impact occurs along an axis of the camera view plane, this allows bubble contour extraction and relevant modal decomposition without bias.

IV. TEMPORAL DYNAMICS OF THE SURFACE MODES

From the moment of film rupture (Fig. 3), the subsequent oscillations of the coalesced bubble clearly originate from an initial highly deformed shape. Therefore, bubble coalescence naturally appears to be an efficient technique to simultaneously excite a large spectrum of shape modes, thus allowing the temporal dynamics of nonspherical bubble oscillations to be studied over a wide range of initial conditions. The modal coefficients $a_n(t)$ obtained from the four bubbles summarized in Fig. 3 and Table I are plotted in Figs. 5 to 8 (blue lines). For the sake of readibility, we limit our analysis to the fourth shape mode, as higher modal amplitudes were negligible in comparison to the predominant nonspherical contribution. Every acquisition covers 15 ms of signal (corresponding to $\sim$500 acoustic periods), from the first image following the film rupture ($t = 0$) to the established steady-state regime. Note that a frame rate of 67.065 kHz and a driving frequency of 31.25 kHz correspond to a sampling of 2.15 frames per acoustic period. Figures 5(a) to 8(a) present a zoom on the first 1.5 ms. The seemingly periodic effect that is visible on the spherical oscillations $R(t)$ in Figs. 5(a) to 8(a) is due to this low sampling and does not have any physical meaning. In order to alleviate the ambiguity on the sampling limitation, a reassigned spectrogram has been performed over the total acquisition length. This spectrogram ensures that the modal amplitudes converge to a steady-state regime. Figures 5(b) to 8(b) present phase-averaged plots of the experimental data during the steady-state regime (typically in the range of 10 ms to 15 ms). These phase-averaged plots also provide direct visualization of the frequency of the nonspherical oscillations. For the selected cases here, this corresponds to the first parametric resonance $f_{ac}/2$ for the second and third shape modes (a_2 in Fig. 6, and a_3 in Fig. 7, respectively) and to the second parametric resonance $2f_{ac}/2 = f_{ac}$ for the fourth shape mode (a_4 in Fig. 8).

A bubble shows spherical oscillations after coalescence if the driving pressure is below the absolute instability threshold (relative to any shape mode). As shown in Fig. 5, all of the shape mode coefficients (notably dominated by a_2) rapidly decay during the transient regime, following classical damped oscillatory behavior, and only the spherical mode $R(t)$ persists in the steady-state regime. As soon as the driving pressure exceeds the instability threshold of a specific shape mode, the corresponding modal coefficient is amplified and persists in the steady-state regime (see Figs. 6 to 8). In all of these cases, the other modal coefficients that correspond to nonresonant shape modes are naturally excited by the large initial deformation (film rupture), but they are rapidly damped until complete disappearance (this is particularly visible in Figs. 7 and 8).

An important feature that is highlighted by the recorded temporal dynamics is the finite-amplitude behavior of the nonspherical oscillations inherent to the possibility of reaching a steady-state regime. As these arise from an unstable mechanism, finite-amplitude nonspherical oscillations necessarily

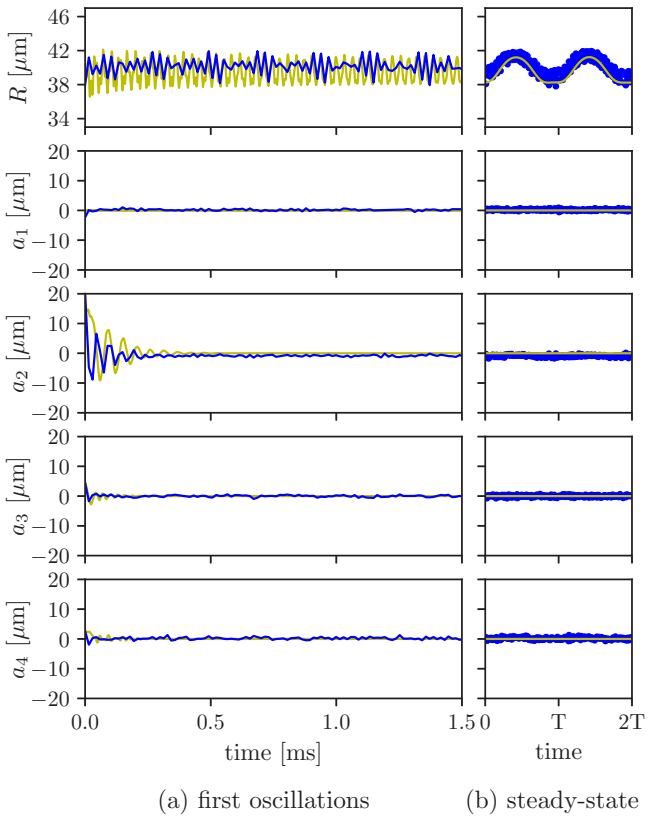

(a) first oscillations (b) steady-state

FIG. 5. Temporal evolution of the radius $R(t)$ and the surface mode coefficients $a_1(t)$ to $a_4(t)$ extracted from the modal decomposition. For this bubble (for parameters, see Table I, row a) only spherical oscillations remain in the steady-state regime, once the surface modes have decayed. Yellow line, simulation; blue line or points, experimental data. (a) The first 1.5 ms of the experiment, starting at the moment of film rupture $t = 0$ ms. (b) During the steady-state regime (in the range 10 ms to 15 ms), with 200 experimental points presented with respect to two acoustic periods $2T = 2/f = 0.064$ ms.

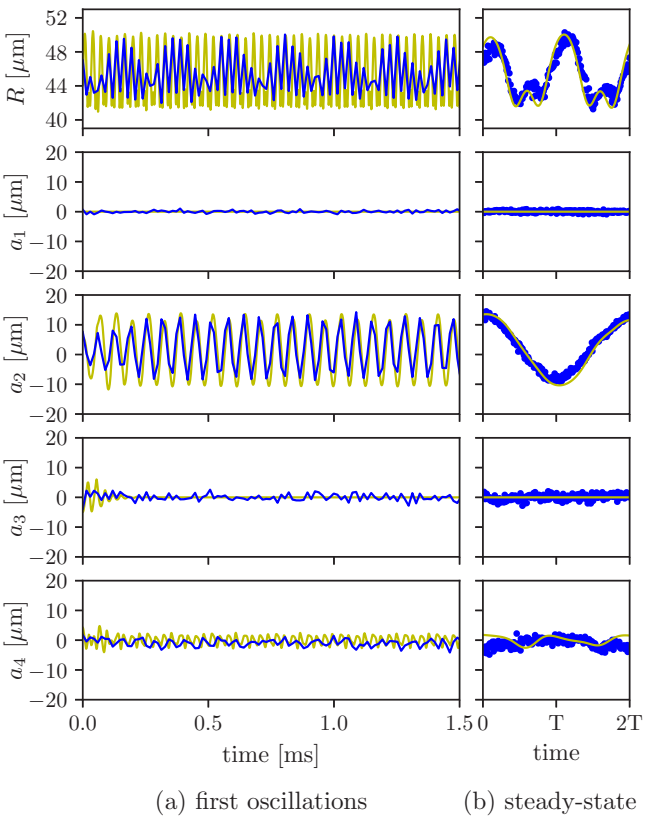

(a) first oscillations (b) steady-state

FIG. 6. As for Fig. 5. This bubble (for parameters, see Table I, row b) shows mode 2 oscillations in the steady-state regime.

imply some kind of saturating processes to counteract the natural exponential growth of the instability. In Figs. 5 to 8, the experimental results are also compared to a model (yellow lines in figures), which allows saturation through nonlinear terms in the dynamical equations [8]. A previous implementation of this model already provided satisfactory comparisons with experimental data [18]. The model is based on a set of dynamic equations that govern the spherical $R(t)$, translational $a_1(t)$, and shape modes $a_n(t)$, for $n \geqslant 2$. The complete set of equations is given in the Appendix, but it can be summarized as follows:

$$R\ddot{R} + \frac{3}{2}\dot{R}^2 = \frac{1}{\rho}\left(p_\infty + \frac{2\sigma}{R_0}\right)\left(\frac{R_0}{R}\right)^{3\gamma} - \frac{p_\infty + p(t)}{\rho} - \frac{2\sigma}{\rho R} - 4\nu\frac{\dot{R}}{R} + H_0\left(\dot{x}^2, a_i^2, \dot{a}_i^2, a_i\dot{a}_i, a_i\ddot{a}_i\right), \quad (3)$$

$$R\ddot{a}_1 + 3\dot{R}\dot{a}_1 + 18\nu\frac{\dot{a}_1}{R} = H_1(a_i a_j, a_i\dot{a}_j, \dot{a}_i\dot{a}_j), \quad (4)$$

$$\ddot{a}_n + B_n\dot{a}_n - A_n a_n = H_n(a_i^2, \dot{a}_i^2, a_i\dot{a}_i, a_i a_j, a_i\dot{a}_j), \quad (5)$$

where ρ and ν are the liquid density and kinematic viscosity, respectively, σ is the surface tension, γ is the gas polytropic index, R_0 is the bubble static radius, and p_∞ and $p(t)$ are the static parts and the acoustic part of the liquid pressure, respectively. A_n and B_n are well-established time-varying coefficients, the expressions for which are given in Refs. [1,18]. In these terms, we added viscosity in a *ad hoc* manner as proposed by Ref. [1]. The functions H_i that appear in Eqs. (4)–(5) gather nonlinear quadratic terms that originate from a perturbative development of the fully nonlinear dynamical equations. Their analytical expressions are lengthy, so the reader is referred to Ref. [8] for complete details. As mentioned above, it is necessary to account for these additional terms to reproduce the saturation and the steady state of the shape oscillations. If these are discarded, Eq. (5) reduces to the well-known parametric equations [1], which admit only either stable (damped) or unstable (exponential growth) solutions.

All of the simulations presented in Figs. 5 to 8 are performed with the following initial conditions. A preliminary simulation of the spherical mode alone (using the experimentally obtained static value R_0 and the acoustic pressure p_{ac}) provides physically reasonable initial conditions for $R(t = 0)$ and its derivative $\dot{R}(t = 0)$. $a_1(t = 0)$ is always assumed to be zero, and $a_2(t = 0)$, $a_3(t = 0)$, and $a_4(t = 0)$ are taken from the experimental decomposition at the moment of film rupture. The shape modes are accounted for up to the fourth mode ($n = 4$) in the simulations. Fairly good agreement between

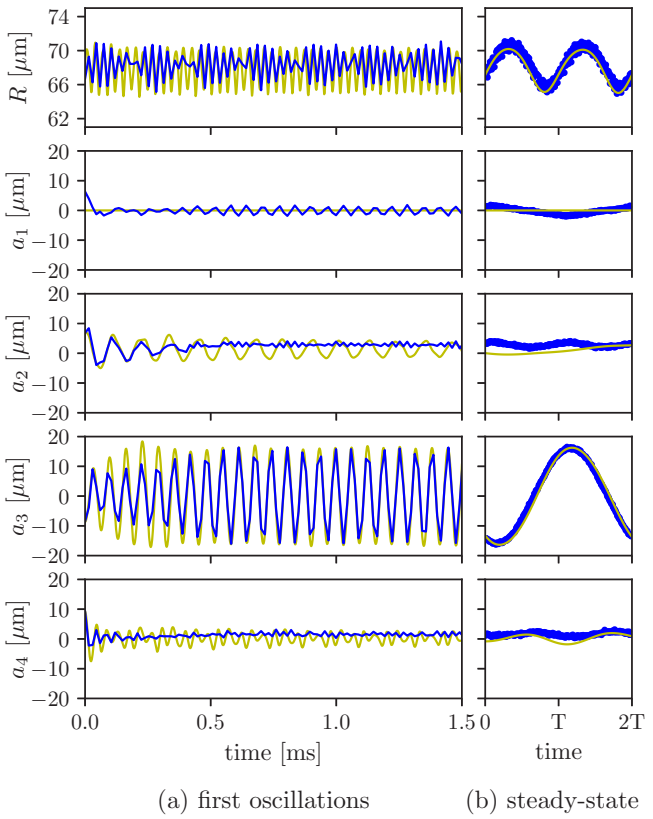

FIG. 7. As for Fig. 5. This bubble (for parameters, see Table I, row c) shows mode 3 oscillations in the steady-state regime.

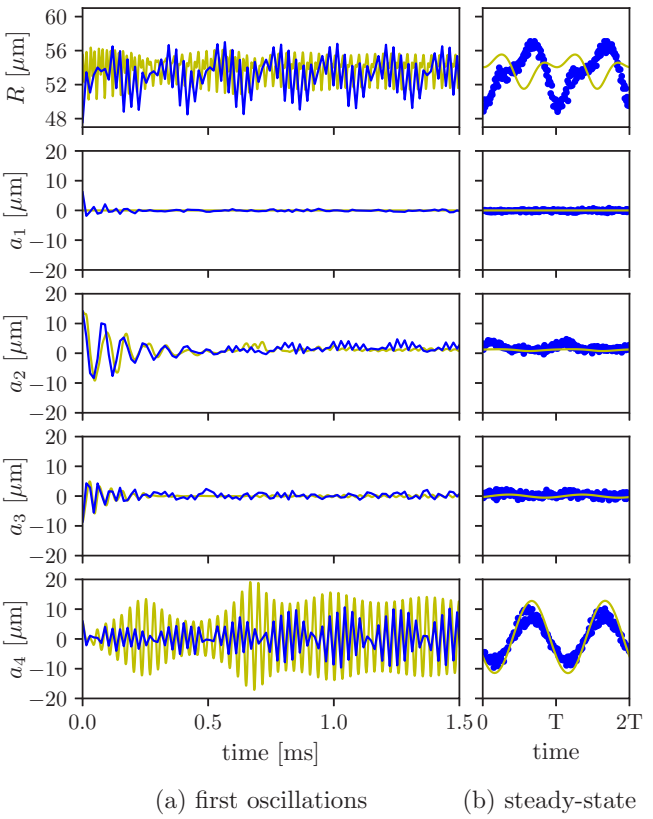

FIG. 8. As for Fig. 5. This bubble (for parameters, see Table I, row d) shows mode 4 oscillations in the steady-state regime.

experiments and theory can be observed in Figs. 5 to 8, including transient regimes with damped oscillations, and steady-state regimes with finite-amplitude shape oscillations. Note that in addition to enabling the establishment of a steady state, the model also predicts amplitudes similar to those observed in the experiments. A discordance can be noted, however, for the bubble that shows a predominant fourth shape mode (Fig. 8), especially looking at the spherical mode coefficient R. This difference can be explained in terms that in addition to lying in the second parametric resonance area of the fourth shape mode, the bubble also comes closer to the second harmonic resonance of the spherical mode. The considered radii and driving pressures lead us to infer that stronger nonlinearities in the bubble dynamics probably make the asymptotic character of the model reach its limits in this particular case. To obtain a stable numerical solution in this particular case, the acoustic pressure of the model has been adjusted to 8.0 kPa, instead of the experimentally obtained 24.1 kPa.

Temporal dynamics of nonspherical oscillations have been investigated in relatively few experimental studies. By modulation of the radiation force, Trinh *et al.* [34] recorded the driven and free-decaying oscillations of trapped bubbles up to a_6 and observed mode coupling. Using short ultrasound pulses, Versluis *et al.* [20] studied the transient dynamics of shape oscillations and reported qualitative agreement with the basic *volume-to-surface* parametric coupling [1]. Similar studies were conducted later on encapsulated bubbles [15,16], although no comparisons with theory have been made. Using low-frequency modulated acoustic driving, Guédra *et al.* [18] showed the periodic on-off of nonspherical oscillations and highlighted mode coupling by providing direct comparisons with the extended theory mentioned above. All of these studies focused on the transient dynamics of the nonspherical oscillations, in contrast to the present data, which allow the establishment of a steady-state regime to be clearly identified. Moreover, because this enables shape modes to be excited over a wide range of initial conditions, the triggering of nonspherical oscillations by bubble coalescence stands out from previous studies that have dealt with initially spherical bubbles or those that were already pulsating upon a given shape mode.

V. CONCLUSIONS

A bubble coalescence technique is used to trigger and sustain nonspherical oscillations of gas bubbles. The originality of this method lies in (1) simultaneous excitation of a large number of shape modes at the moment of impact, (2) control of the bubble orientation and its axis of symmetry defined by the direction of impact, and (3) capture of both the transient and steady-state regimes of bubble dynamics. The first four surface modes are observed experimentally and are consistent with theoretical onset predictions. Finally, the experimental temporal dynamics are compared to numerical simulations, taking into account nonlinear coupling between shape modes. Good agreement was achieved in terms of the transient and steady-state regimes of different shaped modes.

ACKNOWLEDGMENTS

This work was performed within the framework of the Labex CeLyA of the Université de Lyon, within the program Investissements d'Avenir (Grants No. ANR-10-LABX-0060 and No. ANR-11-IDEX-0007) operated by the French National Research Agency (ANR).

APPENDIX: NUMERICAL MODEL

The numerical model we use to compare to our experimental data is based on Ref. [8]. However, we reduce those equations to second order, and we furthermore add viscosity to the first-order terms as specified in Refs. [1,35]. This gives for radial oscillations and translation and surface modes, respectively,

$$0 = \ddot{R}R + \frac{3}{2}\dot{R}^2 + \frac{2\sigma}{\rho R} - \frac{p_b - p}{\rho} + 4\nu\frac{\dot{R}}{R} + \sum_{n=2}^{\infty}\frac{1}{(2n+1)(n+1)}\left[\left(n+\frac{3}{2}\right)\dot{a}_n^2 + (n+3)a_n\ddot{a}_n - (n-3)\right.$$
$$\left.\times\left(\frac{\ddot{R}a_n^2}{R} + \frac{\dot{R}^2a_n^2}{2R^2} + \frac{2\dot{R}a_n\dot{a}_n}{R}\right)\right] - \left[\frac{p_b - p}{\rho} - 3p_b\gamma\left(\frac{R_0}{R}\right)^{3\gamma}\right]\sum_{n=2}^{\infty}\frac{a_n^2}{(2n+1)R^2} - \frac{a_1^2}{4}, \tag{A1}$$

$$0 = R\dot{a}_1 + 3\dot{R}a_1 + 18\nu\frac{a_1}{R^2} - \dot{a}_1\frac{9}{5}a_2 - a_1\left(\frac{9}{5}\dot{a}_2 + \frac{18}{5}\frac{\dot{R}}{R}a_2\right) + \sum_{n=2}^{\infty}\frac{9}{(2n+1)(2n+3)}\left[\frac{2\dot{R}}{R}(\dot{a}_{n+1}a_n - 2n\dot{a}_na_{n+1}) - 2na_na_{n+1}\right.$$
$$\left.\times\left(\frac{\dot{R}^2}{R^2} + \frac{\ddot{R}}{R}\right) + (n+1)\ddot{a}_{n+1}a_n + \dot{a}_{n+1}\dot{a}_n - n\ddot{a}_na_{n+1}\right], \tag{A2}$$

$$0 = R\ddot{a}_n + 3\dot{R}\dot{a}_n + (n-1)\left[-\ddot{R} + (n+1)(n+2)\frac{\sigma}{\rho R^2}\right]a_n + \left[(n+2)(2n+1) - 2n(n+2)^2\frac{\delta}{R}\right]\frac{2\nu}{R}\dot{a}_n$$
$$+\left[(n-1)(n+2) + 2n(n+2)(n-1)\frac{\delta}{R}\right]\frac{2\nu\dot{R}}{R^2}a_n + \frac{9}{4}\delta_{2n}a_1^2 - \frac{3n(n+1)}{2(2n+3)}\dot{a}_1a_{n+1} - \frac{3(n+1)(2n+1)}{2(2n+3)}a_1\dot{a}_{n+1}$$
$$+(1-\delta_{2n})\left[\frac{3n(n+1)}{2(2n-1)}\dot{a}_1a_{n-1} + \frac{3(n+1)\dot{R}}{R}a_1a_{n-1} + \frac{3}{2}(n+1)a_1\dot{a}_{n-1}\right] + \sum_{i=2}^{\infty}\sum_{j=2}^{\infty}\frac{(2n+1)(n+1)}{4}$$
$$\times\left[\frac{\ddot{R}}{R}a_ia_jG_{d_{ijn}} + \frac{\dot{R}^2}{R^2}a_ia_jM_{a_{nij}} + \frac{\dot{R}}{R}\dot{a}_ja_iM_{b_{nij}} + a_i\ddot{a}_jM_{c_{nij}} + \dot{a}_i\dot{a}_jM_{d_{nij}}\right] - \sum_{i=2}^{\infty}\sum_{j=2}^{\infty}a_ia_jI_{a_{nij}}\frac{(2n+1)(n+1)}{2R^2}\frac{p_b - p}{\rho}, \tag{A3}$$

where $G_{d_{ijn}}$, $M_{a_{nij}}$, $M_{b_{nij}}$, $M_{c_{nij}}$, $M_{d_{nij}}$ and $I_{a_{nij}}$ are defined in the appendix of Ref. [8]. As before, R is the radius, a_1 corresponds to translation, and a_n for $n \geqslant 2$ corresponds to the respective surface mode n. σ is the surface tension between the gas contained in the bubble and the surrounding liquid, ρ the density of the liquid, ν the kinematic viscosity in the liquid, and $\delta = \sqrt{\nu/\omega}$ the thickness of the boundary layer, not to be confused with the Kronecker delta δ_{ij}. p is the acoustically induced pressure, which is time-dependent, and $p_b = (p_0 + 2\sigma/R_0) \times (R_0/R)^{3\gamma}$ is the pressure of the bubble at its rest radius R_0 and atmospheric pressure p_0, and we suppose $\gamma = 1.4$.

[1] M. P. Brenner, D. Lohse, and T. F. Dupont, Bubble Shape Oscillations and the Onset of Sonoluminescence, Phys. Rev. Lett. **75**, 954 (1995).

[2] S. Hilgenfeldt, D. Lohse, and M. P. Brenner, Phase diagrams for sonoluminescing bubbles, Phys. Fluids **8**, 2808 (1996).

[3] M. Plesset, On the stability of fluid flows with spherical symmetry, J. Appl. Phys. **25**, 96 (1954).

[4] A. Prosperetti and Y. Hao, Modelling of spherical gas bubble oscillations and sonoluminescence, Philos. Trans. R. Soc., A **357**, 203 (1999).

[5] A. A. Doinikov, Translational motion of a bubble undergoing shape oscillations, J. Fluid Mech. **501**, 1 (2004).

[6] Z. Feng and L. Leal, Bifurcation and chaos in shape and volume oscillations of a periodically driven bubble with two-to-one internal resonance, J. Fluid Mech. **266**, 209 (1994).

[7] C. C. Mei and X. Zhou, Parametric resonance of a spherical bubble, J. Fluid Mech. **229**, 29 (1991).

[8] S. J. Shaw, Translation and oscillation of a bubble under axisymmetric deformation, Phys. Fluids **18**, 072104 (2006).

[9] C. C. Coussios and R. A. Roy, Applications of acoustics and cavitation to noninvasive therapy and drug delivery, Annu. Rev. Fluid Mech. **40**, 395 (2008).

[10] P. Tho, R. Manasseh, and A. Ooi, Cavitation microstreaming patterns in single and multiple bubble systems, J. Fluid Mech. **576**, 191 (2007).

[11] Y. Liu and Q. Wang, Stability and natural frequency of nonspherical mode of an encapsulated microbubble in a viscous liquid, Phys. Fluids **28**, 062102 (2016).

[12] J. Loughran, R. J. Eckersley, and M.-X. Tang, Modeling nonspherical oscillations and stability of acoustically driven shelled microbubbles, J. Acoust. Soc. Am. **131**, 4349 (2012).

[13] K. Tsiglifis and N. A. Pelekasis, Parametric stability and dynamic buckling of an encapsulated microbubble subject to acoustic disturbances, Phys. Fluids **23**, 012102 (2011).

[14] T. A. Spelman and E. Lauga, Arbitrary axisymmetric steady streaming: flow, force and propulsion, J. Eng. Math. **105**, 31 (2017).

[15] B. Dollet, S. M. Van Der Meer, V. Garbin, N. De Jong, D. Lohse, and M. Versluis, Nonspherical oscillations of ultrasound contrast agent microbubbles, Ultrasound Med. Biol. **34**, 1465 (2008).

[16] V. Poulichet, A. Huerre, and V. Garbin, Shape oscillations of particle-coated bubbles and directional particle expulsion, Soft Matter **13**, 125 (2017).

[17] M. Guédra, C. Inserra, B. Gilles, and C. Mauger, Periodic onset of bubble shape instabilities and their influence on the spherical mode, *Ultrasonics Symposium (IUS), 2016 IEEE International* (IEEE, 2016), p. 1.

[18] M. Guédra, C. Inserra, C. Mauger, and B. Gilles, Experimental evidence of nonlinear mode coupling between spherical and nonspherical oscillations of microbubbles, Phys. Rev. E **94**, 053115 (2016).

[19] V. Garbin, D. Cojoc, E. Ferrari, E. Di Fabrizio, M. Overvelde, S. Van Der Meer, N. De Jong, D. Lohse, and M. Versluis, Changes in microbubble dynamics near a boundary revealed by combined optical micromanipulation and high-speed imaging, Appl. Phys. Lett. **90**, 114103 (2007).

[20] M. Versluis, D. E. Goertz, P. Palanchon, I. L. Heitman, S. M. van der Meer, B. Dollet, N. de Jong, and D. Lohse, Microbubble shape oscillations excited through ultrasonic parametric driving, Phys. Rev. E **82**, 026321 (2010).

[21] T. Sanada, A. Sato, M. Shirota, and M. Watanabe, Motion and coalescence of a pair of bubbles rising side by side, Chem. Eng. Sci. **64**, 2659 (2009).

[22] R. Chaudhari and H. Hofmann, Coalescence of gas bubbles in liquids, Rev. Chem. Eng. **10**, 131 (1994).

[23] P. C. Duineveld, The influence of an applied sound field on bubble coalescence, J. Acoust. Soc. Am. **99**, 622 (1996).

[24] R. L. Stover, C. W. Tobias, and M. M. Denn, Bubble coalescence dynamics, AIChE J. **43**, 2385 (1997).

[25] J. Jiao, Y. He, T. Leong, S. E. Kentish, M. Ashokkumar, R. Manasseh, and J. Lee, Experimental and theoretical studies on the movements of two bubbles in an acoustic standing wave field, J. Phys. Chem. B **117**, 12549 (2013).

[26] J. Jiao, Y. He, K. Yasui, S. E. Kentish, M. Ashokkumar, R. Manasseh, and J. Lee, Influence of acoustic pressure and bubble sizes on the coalescence of two contacting bubbles in an acoustic field, Ultrasonics Sonochem. **22**, 70 (2015).

[27] M. Postema, P. Marmottant, C. T. Lancée, S. Hilgenfeldt, and N. de Jong, Ultrasound-induced microbubble coalescence, Ultrasound Med. Biol. **30**, 1337 (2004).

[28] M. Minnaert, XVI. On musical air-bubbles and the sounds of running water, London Edinburgh Dublin Philos. Mag. J. Sci. **16**, 235 (1933).

[29] J. B. Keller and M. Miksis, Bubble oscillations of large amplitude, J. Acoust. Soc. Am. **68**, 628 (1980).

[30] See Supplemental Material at http://link.aps.org/supplemental/10.1103/PhysRevE.98.033115 for original videos showing bubble coalescence leading to microbubbles oscillating in the spherical mode or mode 2, 3 or 4 as well as for information on the experimental conditions.

[31] K. Ohsaka and E. Trinh, A two-frequency acoustic technique for bubble resonant oscillation studies, J. Acoust. Soc. Am. **107**, 1346 (2000).

[32] W. Lauterborn and T. Kurz, Physics of bubble oscillations, Rep. Prog. Phys. **73**, 106501 (2010).

[33] M. Guédra, S. Cleve, C. Mauger, P. Blanc-Benon, and C. Inserra, Dynamics of nonspherical microbubble oscillations above instability threshold, Phys. Rev. E **96**, 063104 (2017).

[34] E. Trinh, D. Thiessen, and R. Holt, Driven and freely decaying nonlinear shape oscillations of drops and bubbles immersed in a liquid: Experimental results, J. Fluid Mech. **364**, 253 (1998).

[35] S. J. Shaw, The stability of a bubble in a weakly viscous liquid subject to an acoustic traveling wave, Phys. Fluids **21**, 022104 (2009).